Supplementary

Employing Cathodoluminescence for Nanothermometry and Thermal Transport Measurements in Semiconductor Nanowires

Kelly W. Mauser[1], Magdalena Solà-Garcia[1], Matthias Liebtrau[1], Benjamin Damilano[2], Pierre-Marie Coulon[3], Stéphane Vézian[2], Philip A. Shields[3], Sophie Meuret[4], Albert Polman[1]*

1. Center for Nanophotonics, NWO-Institute AMOLF, Amsterdam 1098 XG, The Netherlands. 2. Université Côte d'Azur, CNRS, CRHEA, Nice 06103, France. 3. University of Bath, Bath BA2 7AY, United Kingdom. 4. CEMES/CNRS, Toulouse 31055, France..

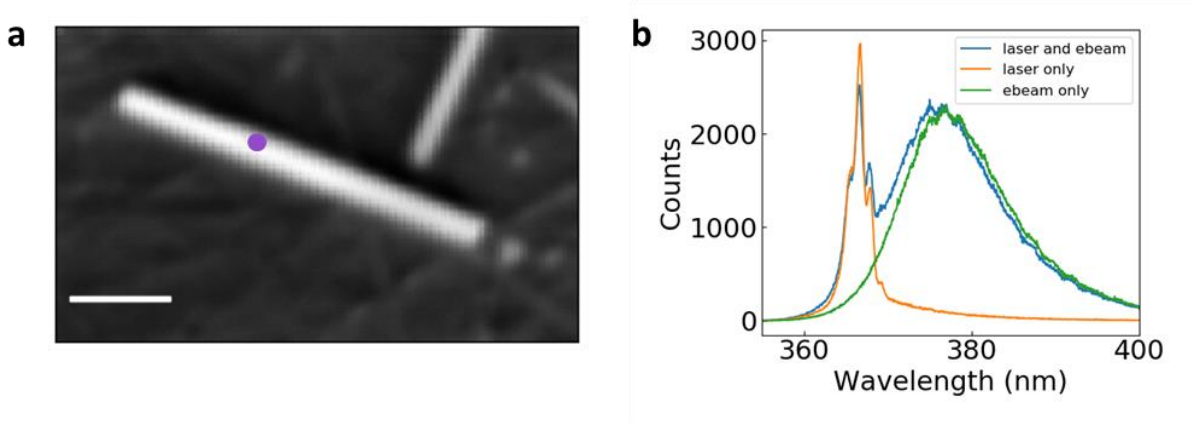

Figure S1. Optically-induced lasing during high current electron beam irradiation. (a) SEM image of GaN nanowire. The shown wire exhibits optical-induced lasing when pumped. The purple dot corresponds to one pixel, with the corresponding CL spectrum shown in (b). Scale bar, 1 μm. (b) Optically induced lasing spectrum (orange, 250 fs, 258 nm laser pulsed at 202 kHz with 1.8 mW average power) from the nanowire in (a), CL spectrum (green, 5 kV, 79 nA) at the location indicated in (a), and spectrum from simultaneous electron beam and laser illumination yielding both CL and optically-induced lasing (blue). The wire showed no noticeable degradation in lasing for over an hour while the electron beam was repeatedly scanned over the wire, indicating that the electrons are not destroying the lasing properties of the wire in a noticeable way. We do observe that the CL yield of the GaN wires does decrease slightly with time after scanning a wire ~30 times or more. We attribute this to electrons filling trap states in GaN in addition to carbon deposition on the surface of the nanowire which increases the surface recombination velocity.[1,2] Whether or not an electron beam damages GaN has been studied previously.[1,2] It has been determined that at the low energies found in an SEM (<30 keV), defects in the atomic lattice are not generated.[3] However, the electron beam can activate existing defects such as Ga vacancies. This, along with charged surface states, can increase the non-radiative recombination rate, yielding a CL intensity that decreases with time until it reaches a

steady state when all defects/states have been activated. Carbon deposition also occurs in an SEM, and while not thick enough to optically block CL, its presence has been found to significantly enhance the surface recombination velocity of GaN. These effects occur at all electron beam currents and are semi-reversible.

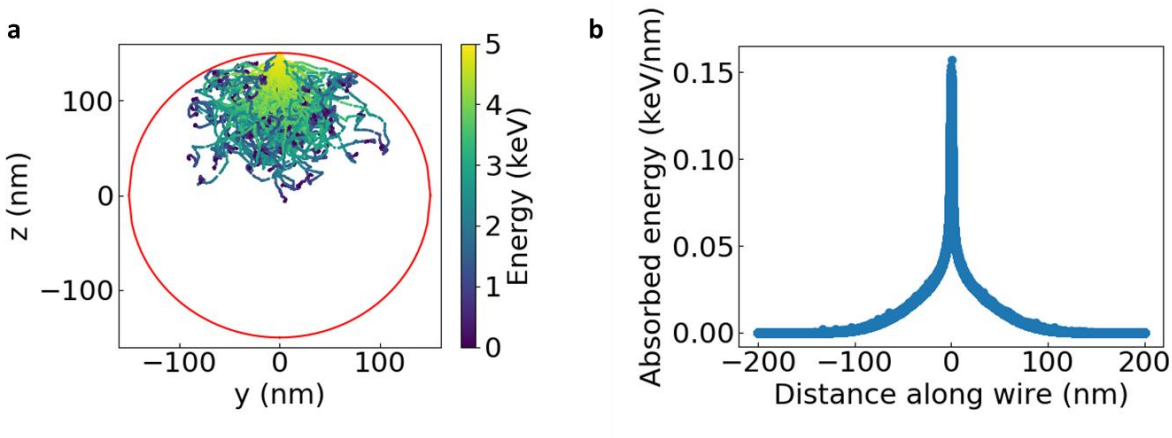

Figure S2. CASINO Monte Carlo simulations of GaN nanowire. (a) Trajectory and energy of 5 keV primary electrons in SEM as calculated by CASINO Monte Carlo simulations in a 150 nm radius GaN wire, outlined in red. (b) Absorbed energy along the long axis of the nanowires as a function of wire length, summed over the cross-sectional area of the wire at point and normalized by number of electrons. The GaN density is 6.15 g/cm^3 and 100,000 5 keV electrons were simulated with a 5 nm incident electron beam diameter. CASINO simulations compute energy lost by an electron while undergoing collisions. We assume energy lost by electrons in the simulation is converted into heat in order to calculate absorbed energy.[4]

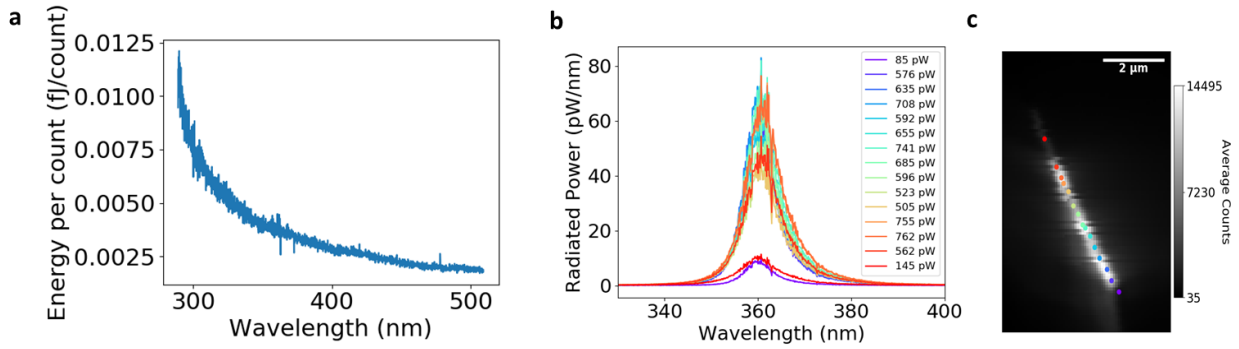

Figure S3. Radiated power from cathodoluminescence as a function of wavelength. (a) Calibration of detector for single crystal aluminum crystal based on a previous method.[5] A theoretical calculation[6] of the energy per unit bandwidth produced by transition radiation from Al per electron was divided by experimental counts from our detector to extract the curve shown. (b) Radiated power spectrum for different pixels with locations corresponding to the dots in (c). Legend gives the total integrated power for each pixel. Power was calibrated using the curve in (a). Slight variations in the system alignment can lead to approximately a 30% change in radiated power in our system[5], therefore the radiated power shown here will have an error of about 30%. As the power deposited in the wire by the electron beam is on the order of hundreds of µWs, radiated power loss from cathodoluminescence is negligible. (c) CL intensity map with colored dots corresponding to the location of the pixel where the spectra in (b) were taken.

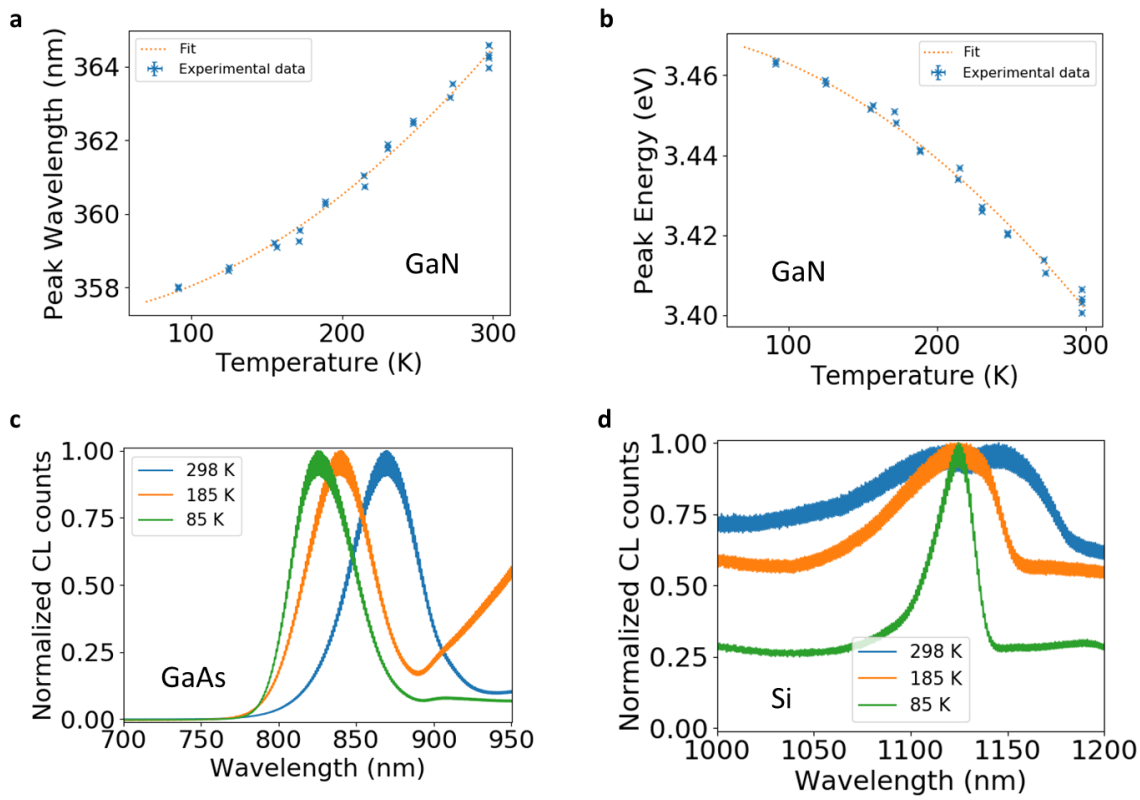

Figure S4. Cathodoluminescence spectral shifts with temperature. (a-b) Calibrated CL peak wavelength and energy *versus* temperature in GaN nanowires scattered on a Si substrate. The electron energy is 5 keV and electron beam current is 548 pA to minimize heating of the nanowires. The CL spectra were fit with a Lorentzian (for simplicity) to determine the peak, and the fit curve is from Equation 1, with constants $E_g(0)$ = 3.471 eV, γ = 2.25×10^3 eV/K, and β = 2609 K. The root mean square error of the data around the line of best fit is 6.0 K. The thermal stage used had temperature accuracy of ± 1 K, and additional error likely comes from doping variations in the wires. (c) Normalized CL spectra at different temperatures for an intrinsic GaAs wafer from 5 keV electrons. (d) Normalized CL spectra at different temperatures for a p-doped Si (5-10 Ω·cm) wafer from 30 keV electrons. GaAs spectra can likely be fit with a Lorentzian in the same manner as GaN to estimate the bandgap shifts, but due to the extensive

broadening of the Si peak in addition to red-shifting of the bandgap, a Voigt or other asymmetric function may be needed to fit the spectra to identify the bandgap shifts. In all plots, the sample is physically and thermally adhered to the SEM thermal stage with silver paste, and the sample temperature is controlled *via* the thermal stage temperature.

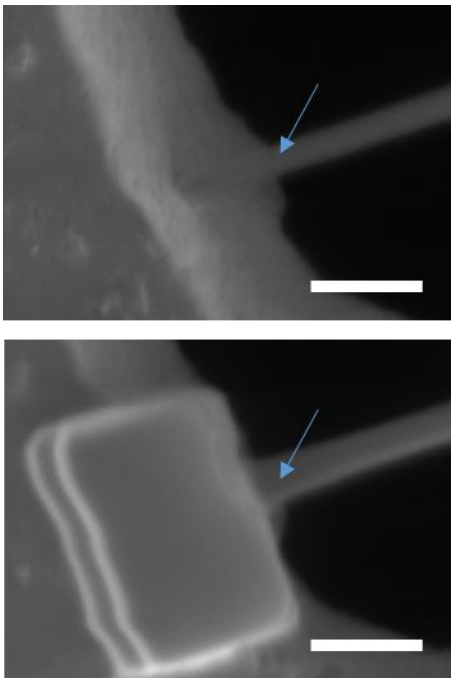

Figure S5. Pt deposition on edges of wires. SEM of nanowire before (top) and after (bottom) Pt was deposited using focused electron-beam-induced deposition. Thickening of the wire near the Pt deposition is apparent (see arrows). Scalebars are 1 μm.

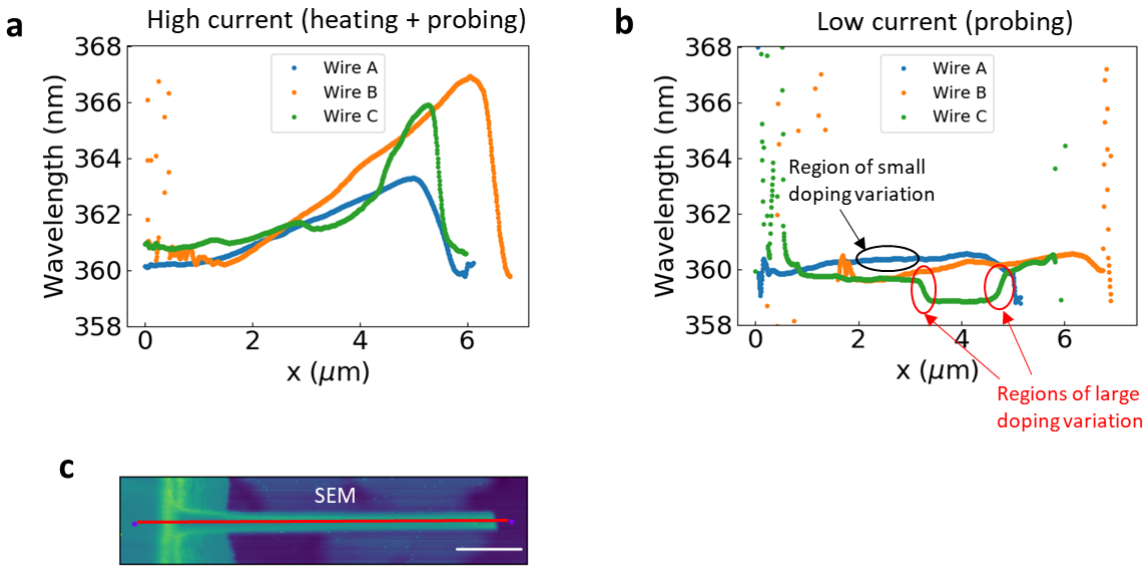

Figure S6. Influence of doping on peak CL wavelength. (a) Uncorrected peak wavelength data corresponding to Wires A (blue), B (orange), and C (green) with temperature data in Figure 3b, along the line shown in the SEM in (c) for a representative wire. The wires were irradiated with 5 keV electrons with beam currents of 15.6, 11.0 and 9.3 nA for Wires A, B, and C, respectively, leading to heating in the wire which causes the redshift in CL emission peak. (b) The same wires measured in (a) are shown measured with electron beam currents of around 1 nA which negligibly heat the wires. Variations in peak wavelength here are presumably caused by variations in doping concentration in the nanowires, as was observed in other nanowires[7]. Red circled regions show locations of large doping variations in Wire C (green), while the black circled region shows a region of relatively little doping variation in Wire A (blue). The large doping variations in Wire C could be responsible for differences in thermal conductivities measured using the DC slope method and AC method. It has been shown that the thermal conductivity of GaN can decrease with increased doping concentration.[8] That study[8] showed a

factor of ~2 or more decrease in thermal conductivity between undoped GaN carrier concentrations (~10^{17} cm^{-1}) and the carrier concentrations found in our nanowires (~10^{18} cm^{-1}). We know that the nanowires used in our study have 2 um of undoped GaN at one end, which we can observe in low-current (non-heating) CL measurements as an approximately 1 nm blue shift in bandgap emission peak and a decrease in CL intensity. For nanowires A, B, and the nanowire used in Figure 3a, this undoped end of the GaN nanowires was the end covered in Pt and heat sunk to the edge of the Cu membrane, leaving the doped portion (with relatively minor doping variations as shown in (b) exposed and probed with the electron beam. Wire C, as seen in (b), has larger doping variations and so could have variations in thermal conductivity along its length, invalidating our models which assume uniform thermal conductivity, although varying thermal conductivity should have been visible in the DC slope analysis by sections of wire with different slope in Figure 3b. In both (a) and (b), peaks and dips of data points at either end of the wire are due to low CL counts and inability of the fitting function to find the peak wavelength. To correct for doping for the DC slope analysis in Figure 3b, an average peak wavelength emission was chosen for a low current cross-cut and deviations from this average were subtracted from the high current cross-cut. Scale bars, 1 μm.

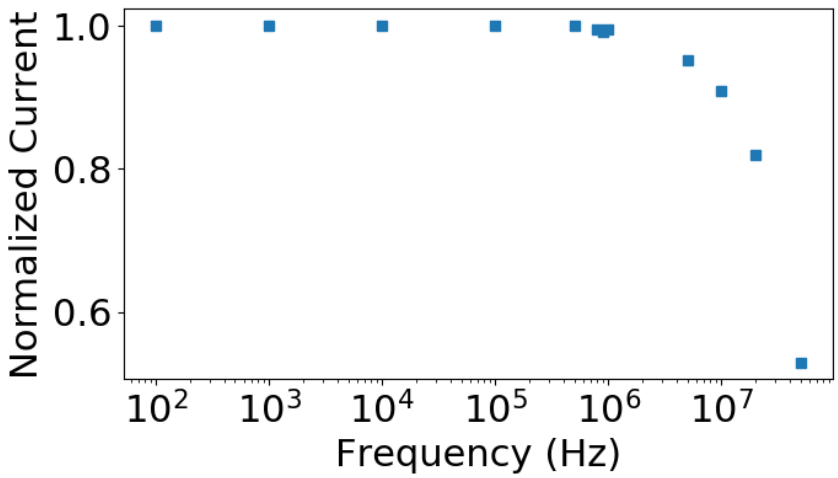

Figure S7. Frequency response of beam blanker. Measured DC electron beam current through a Faraday cup with square wave blanking as a function of frequency using 2 mm blanking plates. The roll-off in current at high frequency is due to the RC time constant of the electrostatic blanking components. The current is normalized to DC current at 100 Hz blanking frequency. The theoretical DC current of the periodically blanked beam should be ½ that of the unblanked beam, which is the case for low frequencies. At 5 MHz, the current has dropped to approximately 95% of the current at 100 Hz.

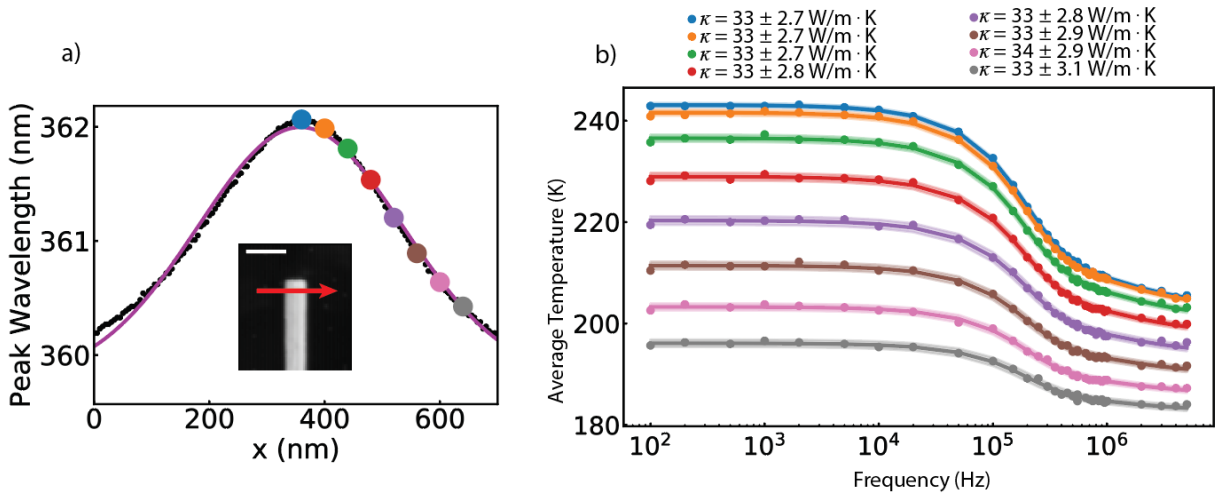

Figure S8. AC thermal conductivity measurements with varying current input. a) Peak wavelength extracted as a function of distance across the end of wire B for a 5 MHz blanked beam. Large apparent wire radius is due to larger electron beam spot size in blanked measurements, as discussed in the manuscript. When the electron beam is centered on the nanowire, more power is deposited, leading to a redshift in the peak wavelength. As the electron beam is scanned further away from the center of the wire, less power is deposited within the nanowire leading to less redshift of the spectrum. Inset is an SEM image taken in continuous mode with better spatial resolution than in blanked measurements. The scale bar is 500 nm. The arrow indicates the approximate path over which the electron beam was scanned over the wire. b) Average temperature as a function of frequency, with each colored line corresponding to the location of the colored dot in a). Shown above plot is extracted thermal conductivity of the wire measured when the electron beam is at given colored point in a) by fitting Equation 5 to the curves in b).

Supplementary Note 1. DC bridge method derivation.

We derive Equation 2 in the paper for the DC bridge method in the following manner. We use a thermal circuit model where $R = \frac{l}{\kappa A}$, where R is thermal resistance, l is length of segment, κ is thermal conductivity of segment, and A is cross-sectional area of segment. In a thermal circuit model, voltage is analogous to temperature difference, ΔT, resistance is analogous to thermal resistance, and current is analogous to heat flux, $\dot{Q}$. The thermal circuit model equivalent of Ohm's law is then $\Delta T = \dot{Q}R$. We fix the temperature at the ends of the wire ($x = 0$ and $x = L$ where L is the total wire length) as T_0. Because Pt partially coats the ends of the wire, as an approximation, we split the wire into 3 different regions. From $x = 0$ to $x = L_1$, the thermal conductivity is κ_0, a mix of the thermal conductivity of Pt and GaN (any effect due to increase of cross-sectional area of this region is incorporated into κ_0). From $x = L_1$ to $x = L_2$, the thermal conductivity is κ_{GaN}. From $x = L_2$ to $x = L$, the thermal conductivity is again κ_0. We neglect thermal contact resistance at the ends of the wires. If we apply a heat flux at location x, we can determine the temperature rise at x by solving the thermal circuit model. We have to consider 3 different cases: when $0 \leq x \leq L_1$, when $L_1 \leq x \leq L_2$, and when $L_2 \leq x \leq L$, as we will need to solve parallel resistance equations and l for each R can change depending on where x is, as will become clear.

For the case of $0 \leq x \leq L_1$, relevant parameters have been shown in Supplementary Fig. S9. To solve for the temperature rise at x, where we also have a heat flux $\dot{Q}$ from the incident electron beam, we need to solve for the total thermal resistance at point x. This appears as two parallel resistance paths to ground. One path is R_A, the other path is $R_B + R_C + R_D$, giving a total resistance of $R_{Total}(x) = \left(\frac{1}{R_A} + \frac{1}{R_B+R_C+R_D}\right)^{-1}$. We use $T(x) - T_0 = \Delta T(x) = \dot{Q}R_{Total}(x)$

to find the first line in Equation 2 in the paper. The other expressions for the cases of $L_1 \leq x \leq L_2$ and $L_2 \leq x \leq L$ can be found in a similar manner.

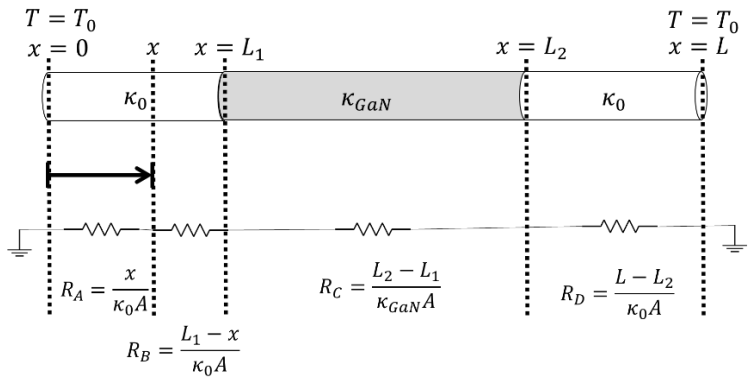

Figure S9. DC bridge method variables for $0 \leq x \leq L_1$. Relevant parameters to compute the temperature profile in the DC bridge method are shown with description in the text. Heat flux $\dot{Q}$ is injected at x from the electron beam.

When we fit our experimental data with Equation 2 in the manuscript, the fit parameters are κ_{GaN}, κ_0, L_1, and L_2.

Supplementary Note 2. Time-dependent 1D temperature profile.

To solve the time-averaged temperature at one end of the GaN wire during the "on" cycle of the electron beam as a function of frequency, we treat the wire as a 1D, uniform system to solve the dimensionless heat equation,

$$u_t = u_{xx}, \quad (S1)$$

where u is temperature deviation from the overall average system temperature. Our dimensionless parameters are $\tilde{t} = \frac{t\kappa}{L^2 C_p \rho}$, $\tilde{x} = \frac{x}{L}$, and $\tilde{\omega} = \frac{\omega L^2 C_p \rho}{\kappa}$, where L is wire length, C_p is heat capacity, ρ is density, and κ is thermal conductivity. Here the dimensionless parameter is used in the equations and the tilde is dropped. The boundary conditions and initial condition are

$$\begin{aligned} &u(x=0,t) = 0, \\ &u_x(x=1,t) = \eta \sum_{m=1,3,5,\ldots}^{\infty} \frac{1}{m} \sin(m\omega t) = \eta \sum_{m=1,3,5,\ldots}^{\infty} \frac{1}{m} \left(\mathrm{e}^{\mathrm{im\omega t}} - \mathrm{e}^{-\mathrm{im\omega t}}\right), \\ &u(x,t=0) = 0. \end{aligned} \quad \text{(S2)}$$

The time-dependent Neumann boundary condition is the Fourier series for a square wave heat input. We expect the heat input to approximate a square wave for frequencies up to approximately 5 MHz before the RC time constant of the electrostatic beam blanker alters the square wave shape (see Figure S7). We expect a solution of the form

$$u(x,t) = v(x,t) + \sum_{m=1,3,5,\ldots}^{\infty} B_m(x) \cos\left(m\omega t + \phi_m(x)\right).$$

Here, $\phi_m(x)$ is the phase term, $v(x,t)$ is the transient component and the second term is the quasi-steady state. We expect the system to reach the quasi-steady state on a much shorter time scale than the exposure time of the spectrometer (10's of ms or longer) due to the small size and

heat capacity of the structure, so the average temperature we read on the spectrometer will be composed of only the second term. We convert this second term, u_{qss}, to the imaginary domain

$$u_{qss}(x,t) = Re\left\{\sum_{m=1,3,5,\ldots}^{\infty} B_m(x)e^{i\phi_m(x)}e^{im\omega t}\right\} = Re\left\{\sum_{m=1,3,5,\ldots}^{\infty} C_m(x)e^{im\omega t}\right\},$$

where C_m is a grouping of all x-dependent terms. Using the identity $Re(z) = \frac{1}{2}(z + z^*)$, where z is a complex number and $z*$ is its complex conjugate, we find

$$u_{qss}(x,t) = \frac{1}{2}\left(\sum_{m=1,3,5,\ldots}^{\infty} C_m(x)e^{im\omega t} + C_m^*(x)e^{-im\omega t}\right)$$

$$= \sum_{m=1,3,5,\ldots}^{\infty} B_m(x)\cos\big(m\omega t + \phi_m(x)\big) \qquad (S3)$$

Putting Equation S3 (center expression) into Equation S1, multiplying by 2, grouping terms, and dropping the sums due to the orthogonality of sines, we find

$$\big(im\omega C_m(x) - C_m''(x)\big)e^{im\omega t} - \big(im\omega C_m^*(x) + C_m''^*(x)\big)e^{-im\omega t} = 0.$$

Using the identity that if $ae^{i\omega t} + be^{-i\omega t} = 0$, then $a = b = 0$, we find

$$im\omega C_m(x) - C_m''(x) = 0 = -\big(im\omega C_m^*(x) + C_m''^*(x)\big). \qquad (S4)$$

We just need to solve one side of this equation, as the left is the complex conjugate of the right side. We then use the boundary conditions in Equation S2 applied to Equation S3 and find that $C_m(0) = 0$ and $C_m'(1) = \frac{A}{im}$. These are the boundary conditions needed to solve Equation S4. We find, noting that $i\omega m = \left(\sqrt{\frac{\omega m}{2}}(1+i)\right)^2$,

$$C_m(x) = d_1 e^{-\sqrt{\frac{\omega m}{2}}(1+i)x} + d_2 e^{-\sqrt{\frac{\omega m}{2}}(1+i)x}$$

where d_1 and d_2 are unknowns we solve for with the $C_m(x)$ boundary conditions we just found. We determine

$$d_1 = -\frac{\frac{\eta}{im}}{\sqrt{\frac{\omega m}{2}}(1+i)e^{\sqrt{\frac{\omega m}{2}}(1+i)} + \sqrt{\frac{\omega m}{2}}(1+i)e^{-\sqrt{\frac{\omega m}{2}}(1+i)}}$$

$$d_2 = \frac{\frac{\eta}{im}}{\sqrt{\frac{\omega m}{2}}(1+i)e^{\sqrt{\frac{\omega m}{2}}(1+i)} + \sqrt{\frac{\omega m}{2}}(1+i)e^{-\sqrt{\frac{\omega m}{2}}(1+i)}},$$

thus,

$$C_m(x) = \frac{\eta}{im}\left(\frac{e^{\sqrt{\frac{\omega m}{2}}(1+i)x} - e^{-\sqrt{\frac{\omega m}{2}}(1+i)x}}{\sqrt{\frac{\omega m}{2}}(1+i)e^{\sqrt{\frac{\omega m}{2}}(1+i)} + \sqrt{\frac{\omega m}{2}}(1+i)e^{-\sqrt{\frac{\omega m}{2}}(1+i)}}\right),$$

and finally,

$$u_{qss}(x,t)$$

$$= Re\left\{\sum_{m=1,3,5,\ldots}^{\infty} \frac{\eta}{im}\left(\frac{e^{\sqrt{\frac{\omega m}{2}}(1+i)x} - e^{-\sqrt{\frac{\omega m}{2}}(1+i)x}}{\sqrt{\frac{\omega m}{2}}(1+i)e^{\sqrt{\frac{\omega m}{2}}(1+i)} + \sqrt{\frac{\omega m}{2}}(1+i)e^{-\sqrt{\frac{\omega m}{2}}(1+i)}}\right)e^{im\omega t}\right\}. \quad (S5)$$

We only measure the temperature when the electron beam is on, or just half a period. Thus, we can integrate Equation S5 over a half period to find the average temperature,

$$\overline{u_{qss}\left(x, t = 0..\frac{\pi}{\omega}\right)}$$

$$= \frac{\omega}{\pi}\int_0^{\pi/\omega} Re\left\{\sum_{m=1,3,5,\ldots}^{\infty} \frac{\eta}{im}\left(\frac{e^{\sqrt{\frac{\omega m}{2}}(1+i)x} - e^{-\sqrt{\frac{\omega m}{2}}(1+i)x}}{\sqrt{\frac{\omega m}{2}}(1+i)e^{\sqrt{\frac{\omega m}{2}}(1+i)} + \sqrt{\frac{\omega m}{2}}(1+i)e^{-\sqrt{\frac{\omega m}{2}}(1+i)}}\right)e^{im\omega t}\right\}dt.$$

Solving, we find

$$\overline{u_{qss}\left(x, t = 0..\frac{\pi}{\omega}\right)}$$

$$= \frac{2\eta}{\pi} Re\left\{\sum_{m=1,3,5,\ldots}^{\infty} \frac{1}{m^2}\left(\frac{e^{\sqrt{\frac{\omega m}{2}}(1+i)x} - e^{-\sqrt{\frac{\omega m}{2}}(1+i)x}}{\sqrt{\frac{\omega m}{2}}(1+i)e^{\sqrt{\frac{\omega m}{2}}(1+i)} + \sqrt{\frac{\omega m}{2}}(1+i)e^{-\sqrt{\frac{\omega m}{2}}(1+i)}}\right)\right\}.$$

Putting the dimensions back into the equation and solving at the end of the wire (x=L), with $\eta = \frac{4\dot{Q}x}{A\kappa\pi^2}$, where $\dot{Q}$ is the power deposited by the electron beam (in Watts) and A is wire cross-sectional area,

$$\overline{T_{qss}\left(L, t = 0..\frac{\pi}{\omega}\right)}$$

$$= \frac{8\dot{Q}x}{A\kappa\pi^2} Re\left\{\sum_{m=1,3,5,\ldots}^{\infty} \frac{1}{m^2}\left(\frac{e^{\sqrt{\frac{\omega L^2 C_p \rho m}{2\kappa}}(1+i)} - e^{-\sqrt{\frac{\omega L^2 C_p \rho m}{2\kappa}}(1+i)}}{\sqrt{\frac{\omega L^2 C_p \rho m}{2\kappa}}(1+i)e^{\sqrt{\frac{\omega L^2 C_p \rho m}{2\kappa}}(1+i)} + \sqrt{\frac{\omega L^2 C_p \rho m}{2\kappa}}(1+i)e^{-\sqrt{\frac{\omega L^2 C_p \rho m}{2\kappa}}(1+i)}}\right)\right\}$$

$$= \frac{8\dot{Q}x}{A\kappa\pi^2} Re\left\{\sum_{m=1,3,5,\ldots}^{\infty} \frac{1}{m^2} \frac{\tanh\left(\sqrt{\frac{\omega L^2 C_p \rho m}{2\kappa}}(1+i)\right)}{\sqrt{\frac{\omega L^2 C_p \rho m}{2\kappa}}(1+i)}\right\}.$$

The full expression for the temperature we should measure with a square wave electron beam parked at the end of the wire, for temperature at the fixed end of T_0, is

$$\bar{T}_{meas}(\omega) = T_0 + \frac{4\dot{Q}L}{A\kappa\pi} + \overline{T_{qss}\left(L, t = 0..\frac{\pi}{\omega}\right)}.$$

References

(1) Campo, E. M.; Hopkins, L.; Pophristic, M.; Ferguson, I. T. Simultaneous Specimen Current and Time-Dependent Cathodoluminescence Measurements on Gallium Nitride. *Journal of Applied Physics* **2016**, *119* (24), 245108.

(2) Lähnemann, J.; Flissikowski, T.; Wölz, M.; Geelhaar, L.; Grahn, H. T.; Brandt, O.; Jahn, U. Quenching of the Luminescence Intensity of GaN Nanowires under Electron Beam Exposure: Impact of C Adsorption on the Exciton Lifetime. *Nanotechnology* **2016**, *27* (45), 455706.

(3) Naresh-Kumar, G.; Bruckbauer, J.; Winkelmann, A.; Yu, X.; Hourahine, B.; Edwards, P. R.; Wang, T.; Trager-Cowan, C.; Martin, R. W. Determining GaN Nanowire Polarity and Its Influence on Light Emission in the Scanning Electron Microscope. *Nano Lett.* **2019**, *19* (6), 3863–3870.

(4) Drouin, D.; Couture, A. R.; Joly, D.; Tastet, X.; Aimez, V.; Gauvin, R. CASINO V2.42—A Fast and Easy-to-Use Modeling Tool for Scanning Electron Microscopy and Microanalysis Users. *Scanning* **2007**, *29* (3), 92–101.

(5) Brenny, B. J. M.; Coenen, T.; Polman, A. Quantifying Coherent and Incoherent Cathodoluminescence in Semiconductors and Metals. *Journal of Applied Physics* **2014**, *115* (24), 244307.

(6) García de Abajo, F. J. Optical Excitations in Electron Microscopy. *Rev. Mod. Phys.* **2010**, *82* (1), 209–275.

(7) Chen, H.-L.; Himwas, C.; Scaccabarozzi, A.; Rale, P.; Oehler, F.; Lemaître, A.; Lombez, L.; Guillemoles, J.-F.; Tchernycheva, M.; Harmand, J.-C.; Cattoni, A.; Collin, S. Determination of *N*-Type Doping Level in Single GaAs Nanowires by Cathodoluminescence. *Nano Lett.* **2017**, *17* (11), 6667–6675.

(8) Florescu, D. I.; Asnin, V. M.; Pollak, F. H.; Molnar, R. J.; Wood, C. E. C. High Spatial Resolution Thermal Conductivity and Raman Spectroscopy Investigation of Hydride Vapor Phase Epitaxy Grown *N*-GaN/Sapphire (0001): Doping Dependence. *Journal of Applied Physics* **2000**, *88* (6), 3295–3300.